1   **Fixation Can Change the Appearance of Phase Separation in Living Cells**

2   Shawn Irgen-Gioro[1,3], Shawn Yoshida[1,2,3], Victoria Walling[1], Shasha Chong[1]*

3   [1] *Division of Chemistry and Chemical Engineering, California Institute of Technology, Pasadena, CA*
4   *91125, USA*

5   [2] *Division of Biology and Biological Engineering, California Institute of Technology, Pasadena, CA 91125,*
6   *USA*

7   [3] *Co-first authors with equal contribution*

8   * Correspondence: schong@caltech.edu

9   **Abstract**

10   Fixing cells with paraformaldehyde (PFA) is an essential step in numerous biological techniques as it is
11   thought to preserve a snapshot of biomolecular transactions in living cells. Fixed cell imaging techniques
12   such as immunofluorescence have been widely used to detect liquid-liquid phase separation (LLPS) *in*
13   *vivo*. Here, we compared images, before and after fixation, of cells expressing intrinsically disordered
14   proteins that are able to undergo LLPS. Surprisingly, we found that PFA fixation can both enhance and
15   diminish putative LLPS behaviors. For specific proteins, fixation can even cause their droplet-like puncta
16   to artificially appear in cells that do not have any detectable puncta in the live condition. Fixing cells in
17   the presence of glycine, a molecule that modulates fixation rates, can reverse the fixation effect from
18   enhancing to diminishing LLPS appearance. We further established a kinetic model of fixation in the
19   context of dynamic protein-protein interactions. Simulations based on the model suggest that protein
20   localization in fixed cells depends on an intricate balance of protein-protein interaction dynamics, the
21   overall rate of fixation, and notably, the difference between fixation rates of different proteins.
22   Consistent with simulations, live-cell single-molecule imaging experiments showed that a fast overall
23   rate of fixation relative to protein-protein interaction dynamics can minimize fixation artifacts. Our work
24   reveals that PFA fixation changes the appearance of LLPS from living cells, presents a caveat in studying
25   LLPS using fixation-based methods, and suggests a mechanism underlying the fixation artifact.

26   **Introduction**

27   Fixing cells to preserve a snapshot of biomolecular transactions *in vivo* is a widely used strategy in
28   numerous techniques in biology and medicine. Due to its small size and high reactivity with a wide range
29   of biological entities, paraformaldehyde (PFA) is one of the most commonly used fixatives to create
30   covalent cross-linking between biomolecules, e.g., proteins and nucleic acids. PFA non-selectively "fixes"
31   or cross-links molecules in proximity to enable characterization of biomolecular interactions formed in
32   living cells. Examples of popular techniques that use PFA to fix cells include ChIP-sequencing (Solomon
33   and Varshavsky, 1985), chromosome conformation capture (3C) based techniques (Quinodoz et al.,
34   2018), immunofluorescence (Richter et al., 2018), fluorescence in situ hybridization (FISH) (Moter and
35   Göbel, 2000), cross-linking mass spectrometry (Sutherland et al., 2008), super-resolution expansion
36   microscopy (Chen et al., 2015), and super-resolution localization microscopies such as stochastic optical
37   reconstruction microscopy (STORM) (Rust et al., 2006). Although PFA fixation has been used to faithfully
38   preserve live-cell conditions in many scenarios, a number of studies have uncovered situations in which
39   fixation fails to cross-link DNA-protein interactions formed in living cells. By imaging different

40 transcription factors (TFs) in live and fixed cells, Schmiedeberg et al. showed that TFs bound to DNA with
41 fast dissociation dynamics (<5 sec residence times as determined by fluorescence recovery after
42 photobleaching (FRAP)) are not cross-linked to DNA upon PFA fixation (Schmiedeberg et al., 2009). Using
43 live-cell single-molecule imaging, Teves et al. showed that TFs stay bound to chromosome during mitosis
44 and fixing cells can artificially deplete transiently bound TFs from mitotic chromosomes (Teves et al.,
45 2016). These studies exemplify the fact that fixation, with limited reaction rates, cannot provide an
46 instantaneous snapshot and may miss or obfuscate biomolecular interactions that happen either at or
47 faster than the timescale of fixation. What further complicates the result of cell fixation is that the
48 reactivity and reaction rates of PFA are variable and dependent on its biomolecule substrates (Gavrilov
49 et al., 2015; Shishodia et al., 2018). For example, the efficiency and rates at which PFA reacts with
50 proteins can vary by orders of magnitude (Kamps et al., 2019) and are dependent on their amino acid
51 sequences (Kamps et al., 2019; Metz et al., 2004; Sutherland et al., 2008) and tertiary structures
52 (Hoffman et al., 2015).

53   Among the numerous biomolecular transactions investigated using fixed cell imaging is liquid-
54 liquid phase separation (LLPS), a long-observed behavior of polymers in solution (Gibbs, 1879; Graham,
55 1861; Hyman et al., 2014) that has recently generated much excitement in biological research
56 communities due to its proposed roles in cellular organization and functions (Banani et al., 2017;
57 Boeynaems et al., 2018; Mitrea and Kriwacki, 2016; Shin and Brangwynne, 2017). LLPS is driven by
58 excessive levels of transient, selective, and multivalent protein-protein interactions mediated by
59 intrinsically disordered regions (IDRs) within the proteins of interest (Chong et al., 2018; Kato and
60 McKnight, 2018; Li et al., 2012). Whereas rigorous characterization of LLPS *in vivo* has been challenging
61 and remains a question under active investigation (McSwiggen et al., 2019b), detection of discrete
62 puncta that have a spherical shape, undergo fusion and fission, and dynamically exchange biomolecules
63 with the surrounding according to FRAP is often considered evidence of putative LLPS in living cells.
64 While such diverse measurements have been widely used for studying proteins under overexpression
65 conditions, far fewer approaches are available to probe LLPS under physiological conditions. Detecting
66 local high-concentration regions or puncta of an endogenously expressed protein using
67 immunofluorescence of fixed cells has been used in many studies as evidence of LLPS (Hayes and Weeks,
68 2016; Kato et al., 2012; Lin et al., 2016; Maharana et al., 2018; Sabari et al., 2018; Wang et al., 2021;
69 Yang et al., 2020). Not only is the detection of puncta an inconclusive metric for establishing LLPS,
70 whether a punctate distribution observed in fixed cells actually represents the live-cell scenario remains
71 unclear, as fixation has only been assumed, but not directly shown, to faithfully preserve multivalent
72 interactions and LLPS formed in living cells. This knowledge gap motivated us to image cells that
73 overexpress various known IDR-containing proteins before and after fixation to evaluate the ability of
74 PFA fixation to preserve LLPS behaviors. We found that interestingly, fixation can significantly alter the
75 appearance of droplet-like puncta in cells. Our quantitative image analysis suggests that depending on
76 the LLPS-driving protein, fixing cells can either enhance or diminish the apparent LLPS behaviors *in vivo*.
77 In certain cases, fixation can even cause droplet-like puncta to artificially appear in cells that have a
78 homogeneous protein distribution and no detectable puncta in the live condition. Conversely, fixation
79 can also cause droplet-like puncta in living cells to completely disappear. Combining experiments that
80 modulate fixation rates, live-cell single-molecule imaging that quantifies protein binding dynamics, and
81 simulations based on a kinetic model, we further demonstrated that protein localization in fixed cells
82 depends on an intricate balance of protein-protein interaction dynamics, the overall rate of fixation, and
83 the difference between protein fixation rates in and out of droplet-like puncta. Our work urges caution

84 in the interpretation of previous claims of *in vivo* phase separation based solely on immunofluorescence
85 imaging of fixed cells and serves to guide future judicious application of PFA fixation.

86 **Results**

87 *Fixation Enhances the LLPS Appearance of FET Family Proteins*

88 To investigate the effect of PFA fixation on the appearance of LLPS, we first compared confocal
89 fluorescence images of live and fixed U2OS cells that transiently express an IDR tagged with EGFP and a
90 nuclear localization sequence (NLS). We focused on the FET family protein IDRs (AA2-214 of FUS, AA47-
91 266 of EWS, and AA2-205 of TAF15) that are reported to undergo putative LLPS in cells upon
92 overexpression (Altmeyer et al., 2015; Chong et al., 2018; Kato et al., 2012; Kwon et al., 2013; Schuster
93 et al., 2020; Wang et al., 2018; Zheng et al., 2020). **Figure 1, Video 1, and Figure 1 - figure supplement 1**
94 compare the same cells before and after treatment of 4% PFA for 10 minutes unless otherwise noted, a
95 typical condition utilized for fixed cell imaging techniques such as immunofluorescence (Stadler et al.,
96 2010). At high enough expression levels, all three IDRs are able to form discrete and spherical puncta in
97 the live cell nucleus, which show fusion and fission behaviors and are thereby consistent with LLPS
98 droplets (Alberti et al., 2019; Banani et al., 2017; Choi et al., 2020; Li et al., 2012). Interestingly, after
99 fixation, the puncta of all three IDRs appear to increase in their numbers, sizes, and contrast compared
100 with the dilute phase. In particular, PFA fixation was able to artificially turn a cell with EGFP-EWS(IDR)
101 homogeneously distributed in the nucleus without any puncta into one with many discrete puncta
102 (**Figure 1A**). We quantified the fixation-induced changes of LLPS appearance by calculating three
103 parameters from the fluorescence images of cells, including the number of puncta, surface roughness,
104 and punctate percentage, and found a significant increase in all three parameters after fixation (**Figure**
105 **1D-F, Figure 1 - source data 1**). The number of puncta and punctate percentage (percentage of
106 intranuclear fluorescence intensity in the concentrated phase) are indicators of the propensity to phase
107 separate (Berry et al., 2015). The surface roughness (standard deviation of pixel intensities across the
108 nucleus) quantifies the uneven distribution of a fluorescently labelled protein in the nucleus, allowing
109 for detection of puncta appearance or disappearance without the need for an algorithm to identify
110 individual puncta in the cell.

111 We next tested how the fixation artifact is dependent on the length of PFA treatment, PFA
112 concentration, and the type of fixatives. We performed real-time imaging of live cells expressing EGFP-
113 FUS(IDR) and found that their morphology and LLPS appearance start to change immediately upon PFA
114 treatment and reach a steady state after ~100 seconds of treatment (**Video 1, Figure 1 - figure**
115 **supplement 2**). We treated cells expressing EGFP-EWS(IDR) with different concentrations of PFA (1%,
116 2%, 4%, and 8%) and observed statistically significant changes to the above three LLPS-describing
117 parameters upon fixation at all the concentrations (**Figure 1 - figure supplement 3**). PFA in combination
118 with glutaraldehyde (GA) has been shown to reduce fixation artifacts in imaging the distribution of cell
119 membrane receptors (Stanly et al., 2016). However, we still observed statistically significant fixation-
120 induced changes to the apparent LLPS behavior of EGFP-EWS(IDR) using 4% PFA and 0.2% GA in
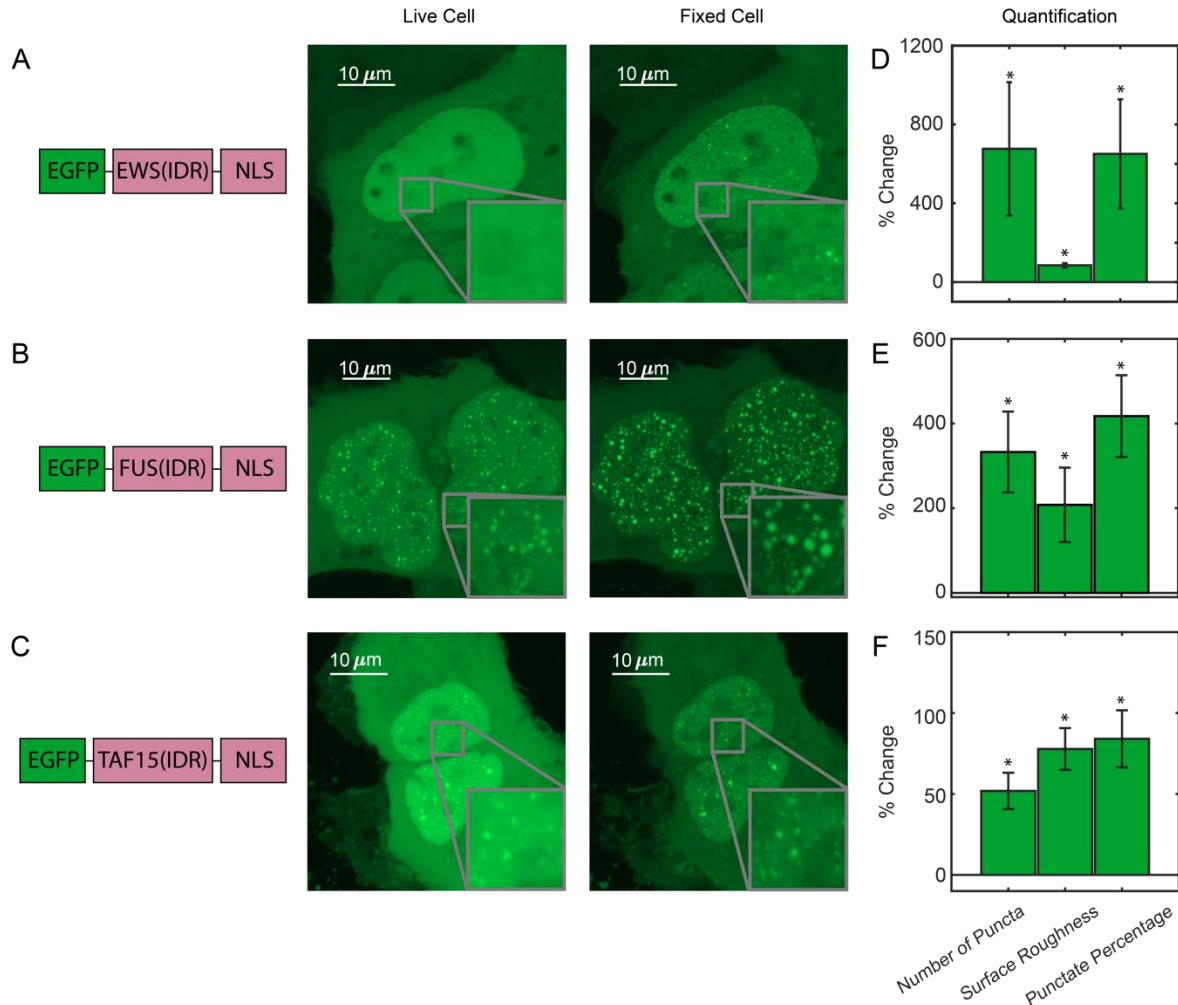121 combination (**Figure 1 - figure supplement 4, figure supplement - source data**).

Figure 1. Fixation can change the apparent LLPS behaviors of proteins. (A) EGFP-EWS(IDR), (B) EGFP-FUS(IDR), (C) EGFP-TAF15(IDR) are transiently expressed in U2OS cells and imaged before and after fixation using confocal fluorescence microscopy. A schematic of each protein construct is shown on the left. Maximum z-projections of representative live cells expressing EGFP-FET family protein constructs are shown next to the same cells after 10 minutes of fixation with 4% PFA. The inserts show a zoomed in region of the cell. (D-F) Quantification of percentage change of LLPS parameters after fixation. The values are averaged from 34 (D), 17 (E), or 24 (F) cells measured in 3 (D), 2 (E), or 2 (F) independent transfection and imaging sessions. Error bars represent standard errors. Asterisks indicate a significant difference compared with 0 (P < 0.05, Wilcoxon signed-rank test).

Figure 1 - source data 1. Quantification of puncta parameters used to generate the bar plots.
Download Figure 1 - source data 1.xlsx

Video 1. **Real-time imaging of a U2OS cell expressing EGFP-FUS(IDR) during PFA fixation.**
122   Download Video1.mp4
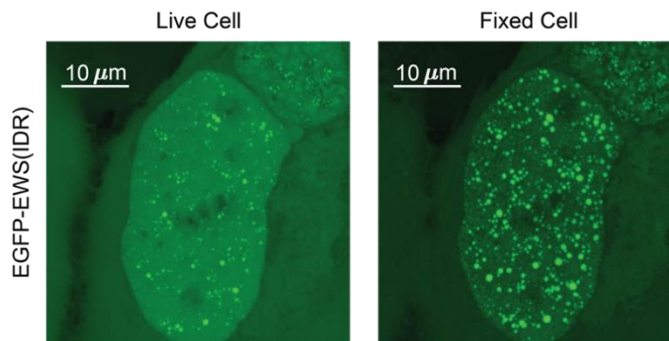
Figure 1 - figure supplement 1. EGFP-EWS(IDR) can form droplet-like puncta in living cells, which change appearance upon fixation. The expression level of EGFP-EWS(IDR) here is significantly higher than in **Figure 1A**. After PFA fixation, additional puncta appear, and pre-existing puncta get bigger and brighter relative to the nucleoplasm, consistent with the trend shown in **Figure 1A**.

123
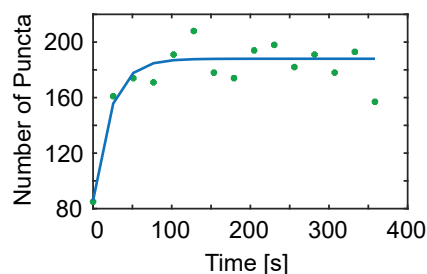
Figure 1 - figure supplement 2. Quantification of Video 1 shows the number of EGFP-FUS(IDR) puncta in the cell as a function of the length of PFA treatment. Fixation is complete in ~100 s. The green scattered plot represents actual data points and the blue line plot is to guide the eye.

124
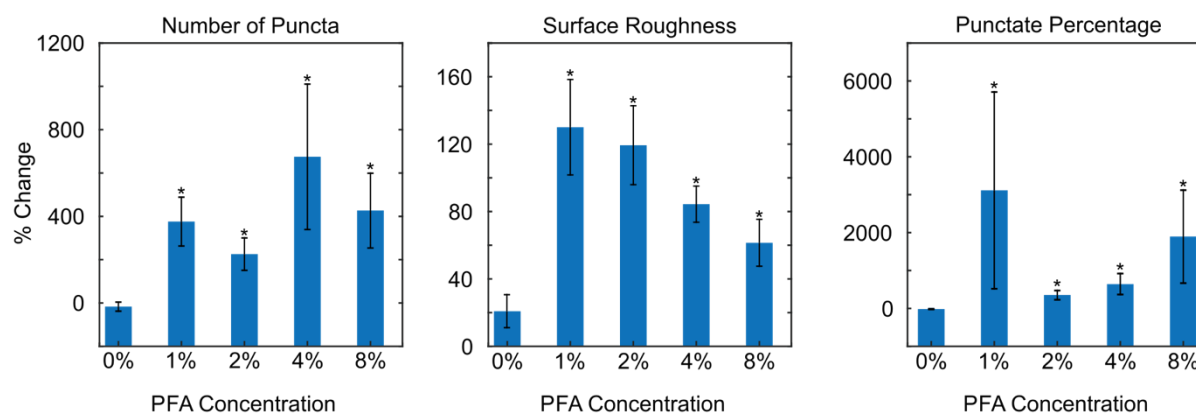
125   **Figure 1 - figure supplement 3. Fixation at various PFA concentrations can change the apparent LLPS**
126   **behaviors of EGFP-EWS(IDR).** We show the percentage change of LLPS parameters after 10 minutes of
127   fixation. The values are averaged from 10 (0% PFA, PBS buffer only), 20 (1% PFA), 20 (2% PFA), 34 (4%
128   PFA), or 20 (8% PFA) cells. Error bars represent standard errors. Asterisks indicate a significant difference
129   of the values compared with 0 ($P < 0.05$, Wilcoxon signed rank test). All the tested concentrations of PFA
130   except for 0% PFA (PBS only) result in a significant change of the LLPS parameters. A quantitative

5

131 comparison between the results at different PFA concentrations is difficult due to increased
132 fluorescence quenching effects at higher concentrations of PFA. We thus focus on comparing the
133 percentage change of LLPS parameters with 0 and with that upon treatment of PBS only.
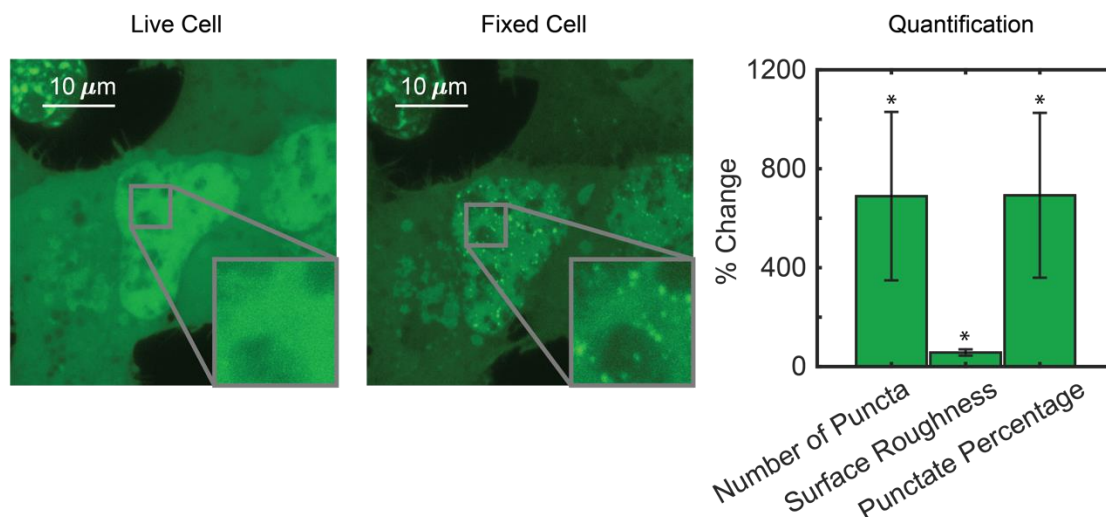
Figure 1 - figure supplement 4. Fixation using PFA/GA in combination still changes the apparent LLPS behaviors of EGFP-EWS(IDR). Adding 0.2% GA to 4% PFA does not reduce the fixation artifact. The fixed cell image was taken 10 minutes after PFA/GA treatment. Percentage change of LLPS parameters after PFA/GA fixation is significantly different from 0, but not significantly different from the percentage change upon PFA only fixation (**Figure 1D**). The values here are averaged from 20 cells measured in one transfection and imaging session. Error bars represent standard errors. Asterisks indicate a significant difference compared with 0 ($P < 0.05$, Wilcoxon signed-rank test).

134

Figure 1 - figure supplement - source data. Quantification of puncta parameters used to generate the supplementary figures 3 and 4.
Download Figure 1 - supplement - source data.xlsx

135
136   We next compared the intracellular distribution of TAF15(IDR) tagged with different fluorescent
137 tags, e.g., EGFP, DsRed2, and HaloTag, before and after fixation with 4% PFA. The LLPS behavior of
138 DsRed2-TAF15(IDR) is enhanced upon fixation like EGFP-TAF15(IDR) (**Figure 2A**), but the enhancement
139 has a different appearance. Whereas there is not a significant change to the large pre-formed DsRed2-
140 TAF15(IDR) puncta, thousands of smaller puncta emerge in the dilute phase within the nucleus (**Figure
141 2B**). In contrast, Halo-TAF15(IDR) displays a diminished LLPS behavior after fixation, with its puncta
142 becoming smaller and dimmer or completely disappearing (**Figure 2C, Figure 2 - figure supplement 1**).
143 Quantification of the number of puncta, surface roughness, and punctate percentage of the TAF15(IDR)
144 LLPS systems before and after fixation further confirmed these observations (**Figure 2D-F, Figure 2 -
145 source data 1**). The fact that different phase-separating proteins can have bifurcating behaviors upon
146 fixation is interesting. While it is known that EGFP and DsRed2 can dimerize and HaloTag cannot (Matz
147 et al., 1999; Sacchetti et al., 2002; Zacharias et al., 2002), it is unclear if and how the dimerization
148 potential might contribute to the proteins' bifurcating responses to PFA fixation. We note that the
149 fixation-induced changes to LLPS appearance can affect the physical characterization of *in vivo* LLPS
150 systems based on fixed cell imaging, such as the Gibbs energy of transfer between dilute and

151 concentrated phases (Riback et al., 2020) and how far from the critical concentration a system is (Bracha
152 et al., 2018), potentially affecting the interpretation of the functional role of LLPS in cellular processes.
153 Moreover, the fact that PFA fixation can artificially promote puncta formation even in cells without
154 detectable puncta in the live condition presents an important caveat in fixation-based approaches that
155 have been commonly used for characterizing LLPS under physiological conditions, e.g.,
156 immunofluorescence (Yu et al., 2021).
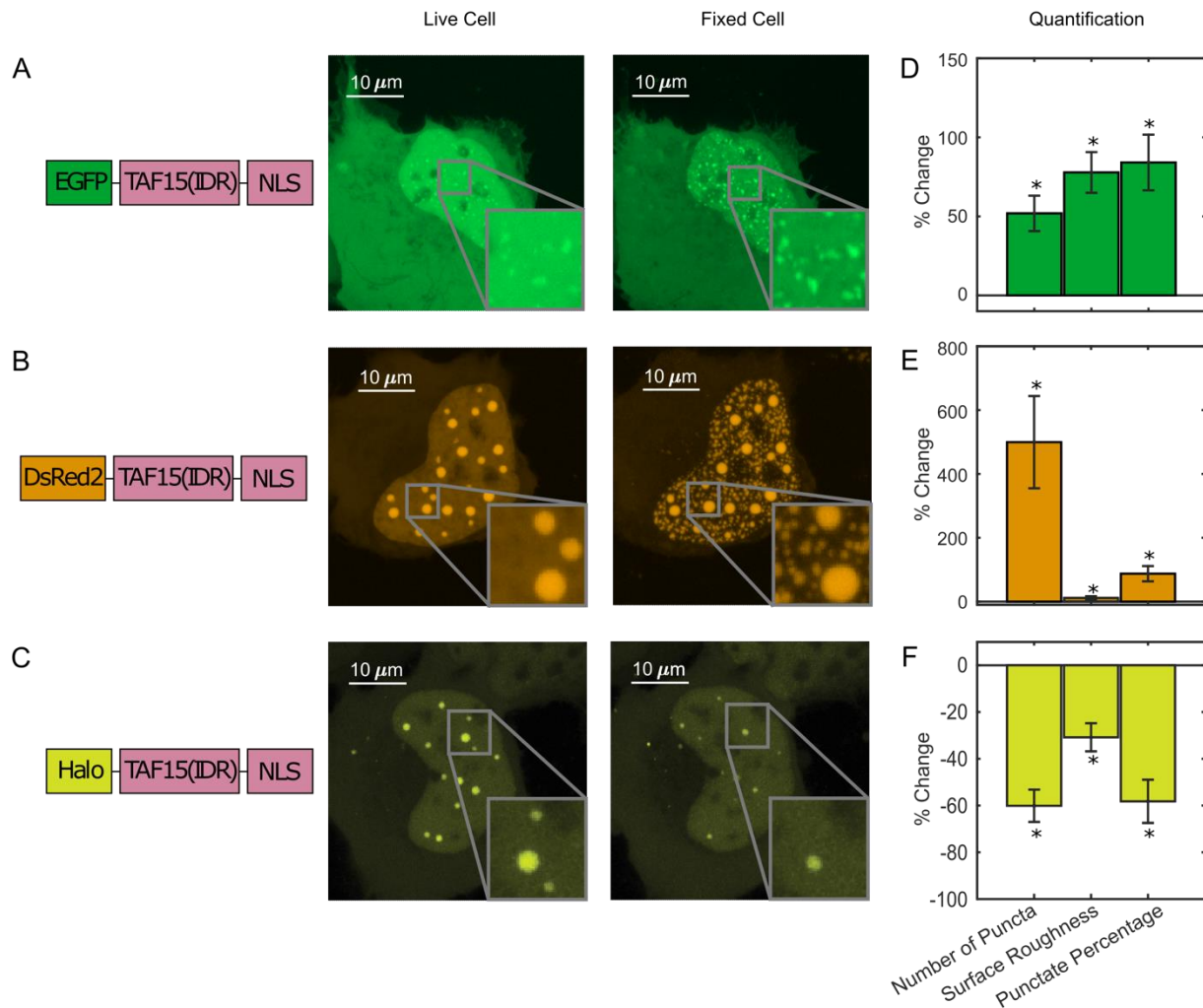
Figure 2. PFA fixation can both enhance and diminish LLPS appearance. U2OS cells expressing (A) EGFP-TAF15(IDR), (B) DsRed2-TAF15(IDR), and (C) Halo-TAF15(IDR), ligated with the JFX549 Halo ligand, are imaged using confocal fluorescence microscopy before and after 10 minutes of fixation with 4% PFA. Schematics of the protein constructs are shown on the left. Live and fixed cell images are compared. (D-F) Quantification of LLPS parameters after fixation. The values are averaged from 24 (D), 23 (E) or 10 (F) cells measured in 2 (D), 2 (E), or 3 (F) independent transfection and imaging sessions. Error bars represent standard errors. Asterisks indicate a significant difference compared with 0 (P < 0.05, Wilcoxon signed-rank test).

157

Figure 2 - source data 1. Quantification of puncta parameters used to generate the bar plots.
Download Figure 2 - source data 1.xlsx
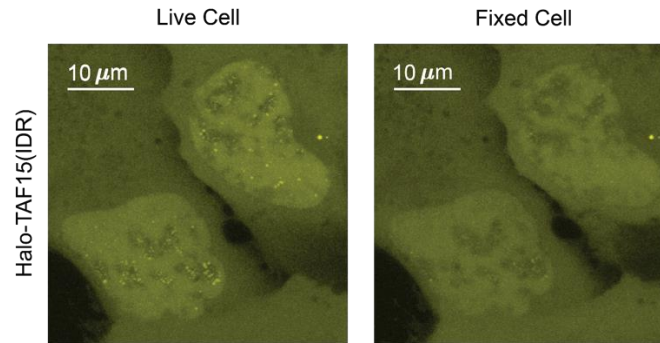
Figure 2 - figure supplement 1. Fixation can diminish LLPS appearance. Two U2OS cells expressing Halo-TAF15(IDR) are side-by-side in the same field of view. Puncta formed in live cell nuclei disappeared after fixation.

158

159   Furthermore, to examine whether all phase-separating proteins show the fixation artifact, we
160   compared live and fixed cell images of EGFP-tagged full-length FUS (FUS(FL)). Full-length FUS is reported
161   to have a greater LLPS propensity *in vitro* than its IDR alone (Wang et al., 2018). We found that EGFP-
162   FUS(FL) overexpressed in live U2OS cells forms many small puncta throughout the nucleus, and we did
163   not observe a significant change of this behavior after PFA fixation (**Figure 3A, Figure 3-Source Data 1**).
164   We also fused Halo-tagged TAF15(IDR) to FTH1 that forms a 24-mer (Bellapadrona et al., 2014 and
165   Bracha et al., 2018) to make an artificial protein with a high LLPS propensity. We found that TAF15(IDR)-
166   Halo-FTH1 overexpressed in live U2OS cells forms large droplet-like puncta and the appearance of LLPS
167   does not significantly change after PFA fixation (**Figure 3B, and Figure 3 - source data 1**). In addition, we
168   looked into a native IDR-containing protein, EWS::FLI1, an oncogenic TF causing Ewing sarcoma
169   (Grünewald et al., 2018) and known to form local high-concentration hubs at target genes associated
170   with GGAA microsatellites (Chong et al., 2018). Although there is no convincing evidence that EWS::FLI1
171   undergoes LLPS under physiological conditions, the formation of its hubs is mediated by the homotypic
172   multivalent interactions of EWS(IDR) within the protein. Excessive levels of such multivalent interactions
173   often result in LLPS (Li et al., 2012). We previously Halo-tagged endogenous EWS::FLI1 in an Ewing
174   sarcoma cell line A673 using CRISPR/Cas9-mediated genome editing (Chong et al., 2018). Here, we
175   compared live and fixed A673 cell images of endogenous EWS::FLI1-Halo and did not observe a
176   significant difference in its distribution (**Figure 3C, Figure 3 - source data 1**). This result suggests that PFA
177   fixation does not change the intracellular distribution of all proteins that have a LLPS potential.

Figure 3. Not all puncta-forming proteins show the fixation artifact. U2OS cells expressing (A) EGFP-FUS(FL) and (B) TAF15(IDR)-Halo-FTH1, and (C) an A673 cell expressing endogenous EWS::FLI1-Halo are imaged using confocal fluorescence microscopy before and after 10 minutes of fixation with 4% PFA. Halo-tagged proteins are ligated with the JFX549 Halo ligand before imaging. Schematics of the protein constructs are shown on the left. Live and fixed cell images are compared. (D-F) Quantification of puncta parameters after fixation. The values are averaged from 21 (D), 16 (E), or 15 (F) cells measured in 1 (D), 4 (E), or 2(F) independent transfection and imaging sessions. Error bars represent standard errors. NS: not significant difference compared with 0 (P < 0.05, Wilcoxon signed-rank test). None of the examined proteins show significant changes in their LLPS or hub appearance in the fixed cell image as compared to the live cell image.

178

Figure 3 - source data 1. Quantification of puncta parameters used to generate the bar plots.
Download Figure 3 - source data 1.xlsx

179

180   *Switching between Enhancing and Diminishing the LLPS Appearance Depends on Fixation Kinetics*

181   To understand what factors are underlying the diverging fixation artifact of *in vivo* LLPS systems, we
182   perform the above-described fixation imaging assay with glycine added to live cells prior to PFA fixation.
183   Glycine is highly reactive with formaldehyde and is commonly used to quench the formation of protein-
184   protein cross-linked complexes by quickly forming protein-glycine and glycine-glycine cross-linked
185   adducts instead (Hoffman et al., 2015). We thus utilized additional glycine to generate a competitive

186 fixation reaction in the cell against protein-protein fixation. We found that adding 25mM glycine to live
187 U2OS cells that overexpress DsRed2-TAF15(IDR) increases the starting punctate percentage from $18 \pm$
188 1.92 to $36 \pm 3.82\%$ (quantified from 23 cells), indicating an increase in the degree of LLPS. Although the
189 underlying mechanism of such increase is unclear, we speculate this might be because hydrophobic
190 intermolecular contacts that play an important role in TAF15(IDR) LLPS (Patel et al., 2017) are enhanced
191 by the presence of hydrophobic glycine. Importantly, addition of glycine dramatically reversed the
192 fixation effect on the LLPS behavior of DsRed2-TAF15(IDR). Whereas PFA fixation in the absence of
193 additional glycine enhances the LLPS appearance (**Figure 2B and Figure 4A**), in the presence of 25mM
194 glycine, fixation causes many of the smaller puncta formed in live cells to disappear completely and
195 larger, pre-formed puncta to turn into a "donut" shape, with the outline of the puncta still visible but
196 the interior devoid of the protein (**Figure 4B**). None of these fixed-cell images are good representations
197 of live cells, but it appears that glycine affects the critical parameters that control the divergent artifact
198 of PFA fixation. The observation that the appearance of droplet-like puncta in fixed cells can be
199 dramatically modified by the presence of glycine competition emphasizes that the kinetics of fixation
200 can play an essential role in the appearance of LLPS in fixed cells.
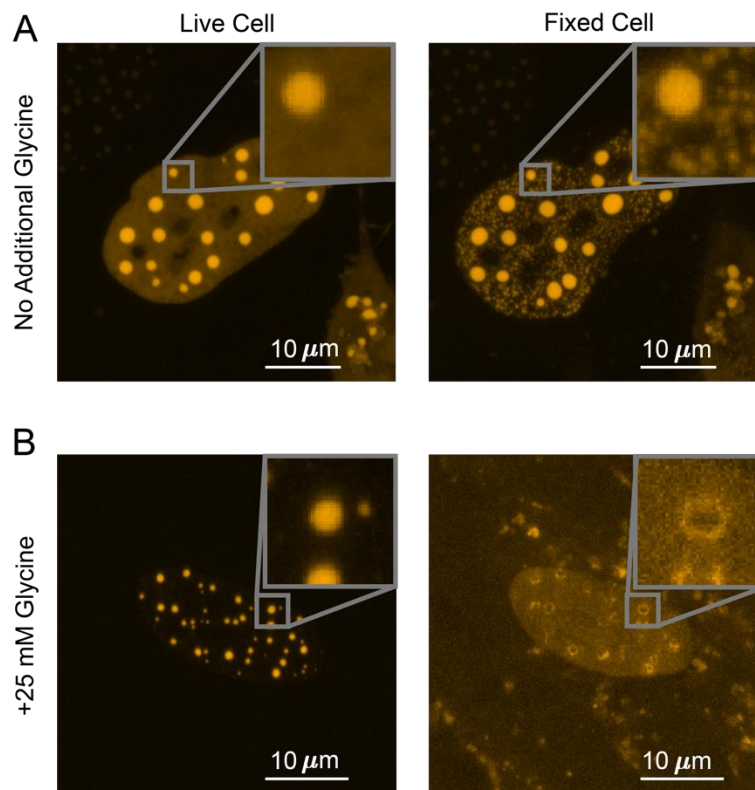
Figure 4. Competitive fixation pathway creates a reversed fixation artifact. (A) Fixing U2OS cells that express DsRed2-TAF15(IDR) in the absence of additional glycine causes many small puncta to appear. (B) Fixing cells in the presence of 25 mM additional glycine results in a reduction in the number of puncta, with large puncta forming "donut" shapes. In both (A) and (B), cells are imaged using confocal fluorescence microscopy before and after 10 minutes of fixation with 4% PFA.

201   *Kinetic Modeling Explains the Fixation Artifact*

202   Given our observation that fixation kinetics are critical to the appearance of LLPS in fixed cells, we
203   numerically simulated a 4-state kinetic model (Hoops et al., 2006). As shown in **Figure 5A-B**, the model
204   focuses on one protein of interest (POI), which before fixation can either be in state S_1 - "in puncta" or
205   S_2 - "out of puncta". Because POI molecules are dynamically exchanged in and out of puncta, the in-
206   puncta percentage (punctate percentage) of POI is at an equilibrium determined by the ratio of the
207   binding rate, k_1, and the dissociation rate, k_2 (Pollard, 2010). These are the average exchange rates
208   between S_1 and S_2 and do not concern the potential spatial inhomogeneity in the rates at the molecular
209   level. For example, individual POI molecules at the surface and interior of a punctum might dissociate
210   with different rates, but our model does not differentiate these molecules. We define the moment that
211   PFA is added as time zero ($t = 0$) and introduce two fixed states of POI, which are S_3 (POI cross-linked to
212   proteins within puncta) with a fixation rate of k_3 and S_4 (POI cross-linked to proteins outside puncta)
213   with a fixation rate of k_4. Because fixing to both S_3 and S_4 states are irreversible, when the cell is fully
214   fixed long after addition of PFA ($t = \infty$), there is no longer any concentration in S_1 and S_2. The fixation
215   artifact of an LLPS system can be represented as the absolute change in punctate percentage, or the
216   ratio of in-puncta POI to total POI, after fixation:

$$\Delta Punctate\ Percentage = Final\ Punctate\ Percentage - Initial\ Punctate\ Percentage \quad (1)$$

$$= \left(\frac{[S_3]_{t=\infty}}{[S_3]_{t=\infty} + [S_4]_{t=\infty}} - \frac{[S_1]_{t=0}}{[S_1]_{t=0} + [S_2]_{t=0}} \right) * 100$$

217   We hypothesized that the balance between interaction and fixation dynamics in a LLPS system causes
218   the fixation artifact and tested the hypothesis by calculating $\Delta Punctate\ Percentage$ as a function of
219   various kinetic and equilibrium parameters.

220   It is well-established that the dilute and concentrated phases of a LLPS system have different
221   protein composition and concentrations (Currie and Rosen, 2022; Koga et al., 2011; Magdalena Estirado
222   et al., 2020; Nott et al., 2015; Yewdall et al., 2021). The rate of fixation is known to vary with both
223   factors by orders of magnitude, with the timescale of fixation ranging from seconds to hours (Hoffman
224   et al., 2015; Kamps et al., 2019; Metz et al., 2006; Metz et al., 2004). Because protein-protein
225   interactions that drive LLPS are highly dynamic with binding residence times in the range of seconds to
226   tens of seconds (Chong et al., 2018), fixation likely happens with either lower or comparable rates than
227   protein binding and dissociation. We thus first examined if different fixation rates of POI in and out of
228   puncta can cause a fixation artifact, assuming the overall fixation rates ($k_3 + k_4$) are slower than protein
229   binding and dissociation, and how the fixation artifact may depend on intrinsic protein-protein
230   interaction equilibrium. Specifically, we calculated $\Delta Punctate\ Percentage$ as a function of the starting
231   punctate percentage and the relative in-puncta fixation rate (k_3:k_4) when the relative overall fixation
232   rate is constant (($k_3 + k_4$):($k_1 + k_2$)=1:5) (**Figure 5C**). In the scenario where the rate of fixation is the
233   same in and out of the puncta ($k_3 = k_4$), the live-cell equilibrium is perfectly preserved in fixed cells
234   regardless of the starting punctate percentage ($\Delta Punctate\ Percentage \sim 0$). However, when one
235   fixation rate is faster than the other, we observe a bifurcating effect. When the fixation rate inside the
236   puncta is greater than outside the puncta ($k_3 > k_4$), the fixed cell will have a higher punctate percentage
237   than the live cell, i.e., fixation enhances the apparent LLPS behaviors. When the balance is reversed
238   ($k_4 > k_3$), the fixed cells will have diminished apparent LLPS behaviors than in the live cell. For cases

239 where the starting punctate percentage is near 0% or 100% due to significantly different POI binding and
240 the dissociation rates ($k_2 \gg k_1$ or $k_1 \gg k_2$), no significant change to LLPS appearance happens after
241 fixation ($\Delta Punctate\ Percentage \sim 0$). In short, our simulation suggests that having unequal fixation
242 rates in and out of puncta is necessary to cause a fixation artifact of LLPS systems and the artifact is
243 dependent on the punctate percentage of POI in living cells.
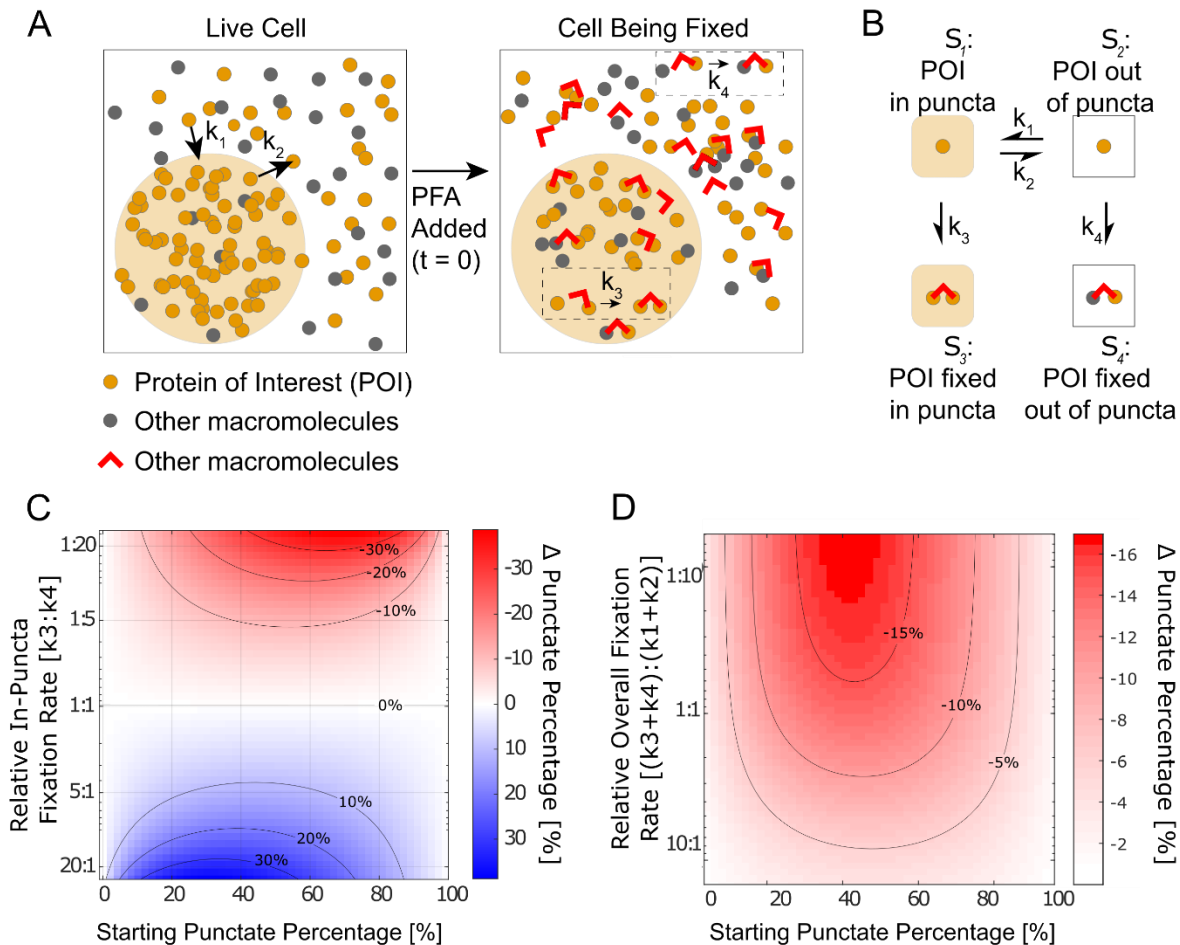
Figure 5. **Kinetic simulation explains bifurcating fixation artifacts**. (A) Schematic that describes fixation of a phase-separating POI in the cell. (B) The four-state kinetic model with associated kinetic rates connecting the different states. (C) Simulation of the fixation artifact as a function of the starting punctate percentage and the relative in-puncta fixation rate $k_3 : k_4$, assuming the overall fixation rate as well as overall protein binding and dissociation rates are constant ($k_3 + k_4 = 0.2$, $k_1 + k_2 = 1$). Faster in-puncta fixation causes LLPS behavior to be over-represented (blue). Slower in-puncta fixation causes LLPS behavior to be under-represented (red). (D) Simulation of the fixation artifact as a function of the starting punctate percentage and the relative overall fixation rate $(k_3 + k_4):(k_1 + k_2)$, assuming individual fixation rates are constant ($k_3 = 1$, $k_4 = 2$). Fast overall fixation rate compared with protein-protein interaction dynamics decreases the fixation artifact. (C) and (D) were simulated over starting punctate percentages ranging from 0% ($k_1 = 0$, $k_2 = 1$) to 100% ($k_1 = 1$, $k_2 = 0$). Level curves are marked on (C) and (D).

244

12

245   Because previous reports have documented that fixation preserves transient interactions worse
246   than stable interactions (Poorey et al., 2013; Schmiedeberg et al., 2009; Teves et al., 2016), we next
247   investigated how fixation rates relative to protein-protein interaction dynamics may impact the
248   observed fixation artifact. Specifically, we calculated $\Delta Punctate\ Percentage$ as a function of both the
249   starting punctate percentage and the relative overall fixation rate, $(k_3 + k_4):(k_1 + k_2)$, assuming a
250   constant relative in-puncta fixation rate ($k_3: k_4$ =1:2) (**Figure 5D**). Here, a fast relative overall fixation
251   rate can either be caused by slow protein-protein interaction dynamics (low $(k_1 + k_2)$) or fast absolute
252   fixation rates (high $(k_3 + k_4)$). We found when the protein-protein interactions are highly dynamic
253   compared with the overall fixation rates ($(k_3 + k_4) \ll (k_1 + k_2)$), the fixation artifact is the most
254   pronounced as shown by a large value of $\Delta Punctate\ Percentage$. In contrast, when the protein-
255   protein interactions are stable and less dynamic compared with the overall fixation rate ($(k_3 + k_4) \gg$
256   $(k_1 + k_2)$), there is a minimal fixation artifact and the punctate percentage in fixed cells is similar to that
257   in living cells ($\Delta Punctate\ Percentage \sim 0$). In short, our simulation suggests that when the overall
258   fixation rate is fast compared with the dynamics of targeted interactions, fixation artifacts can be
259   minimized even with unequal fixation rates in and out of puncta.

260   Overall, our kinetic model suggests that the observed fixation artifact of LLPS systems is driven
261   by the interplay of three factors: protein-protein interaction dynamics, the absolute overall fixation rate,
262   and different fixation rates in and out of puncta. Different fixation rates of POI in and out of puncta
263   ($k_3: k_4 \neq 1: 1$) are required for fixation artifacts to happen and the value of $k_3: k_4$ determines whether
264   the LLPS behavior of POI gets over-represented or under-represented in fixed cell images. The intrinsic
265   rates by which POI binds to and dissociates from its puncta impact the magnitude of fixation artifacts by
266   determining both the live-cell equilibrium of LLPS (starting punctate percentage) and the relative overall
267   fixation rate of POI ($(k_3 + k_4):(k_1 + k_2)$).

268   *A Fast Overall Fixation Rate Relative to Binding Dynamics Can Minimize Fixation Artifacts*

269   As discussed above, our model suggests that when the overall fixation rate is fast compared with the
270   dynamics of targeted protein-protein interactions, fixation artifacts can be minimized even with unequal
271   fixation rates in and out of puncta. In order to test this prediction experimentally, we focused on Halo-
272   TAF15(IDR), which exhibits significantly diminished LLPS behavior upon fixation (**Figure 2C**), and
273   TAF15(IDR)-Halo-FTH1, which does not exhibit a significant fixation artifact (**Figure 3B**). The fact that
274   fixation of both Halo-TAF15(IDR) and TAF15(IDR)-Halo-FTH1 are completed within 1~2 minutes suggests
275   comparable overall fixation rates of the two proteins. Thus, our model predicts that TAF15(IDR)-Halo-
276   FTH1 has more stable homotypic interactions than Halo-TAF15(IDR), resulting in a higher relative overall
277   fixation rate of the former than the latter. To test this prediction, we performed live-cell single-molecule
278   imaging of Halo-TAF15(IDR) and TAF15(IDR)-Halo-FTH1 and measured their binding residence times
279   (RTs) at respective droplet-like puncta. Using established single-particle tracking (SPT) analysis (Chong et
280   al., 2018), we found the RTs of TAF15(IDR) and TAF15(IDR)-FTH1 to be 10.23 $\pm$ 1.10 and 64.15 $\pm$
281   11.65 seconds, respectively (**Figure 6, Figure 6 - source data 1**). This result suggests significantly more
282   stable binding of TAF15(IDR)-FTH1 than TAF15(IDR). Together, these imaging data are consistent with
283   our model's prediction that a fast overall fixation rate relative to binding dynamics can minimize fixation
284   artifacts.

285
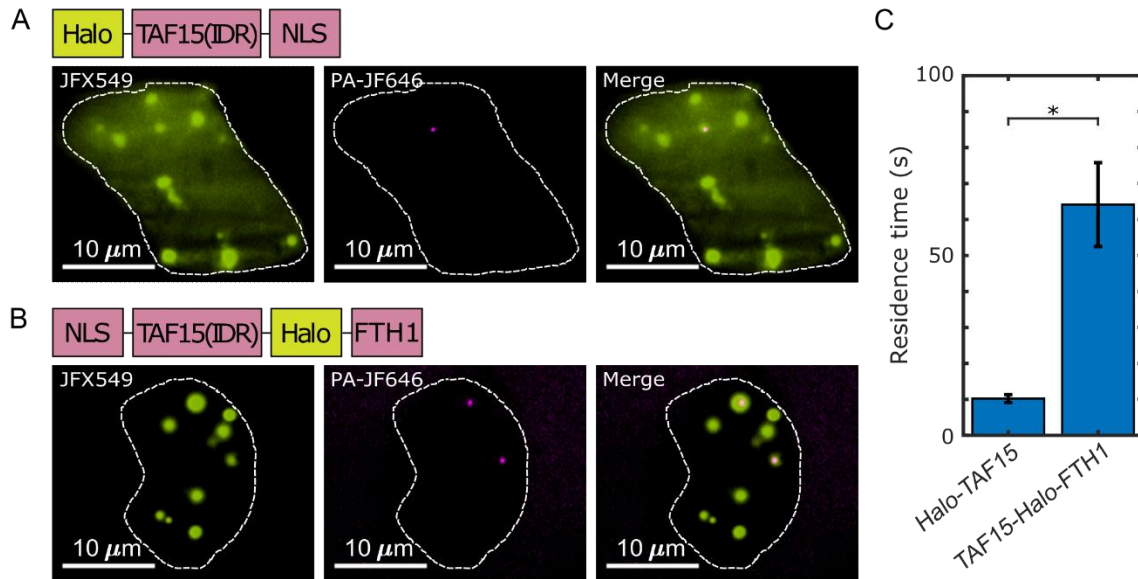
Figure 6. **The residence times of proteins in their droplet-like puncta vary**. Shown are individual frames from two-color single-molecule movies of (A) Halo-TAF15(IDR) and (B) TAF15(IDR)-Halo-FTH1. Each protein was labelled with a lower concentration of a photoactivatable dye for SPT (20 nM PA-JF646, magenta) and a higher concentration of non-photoactivatable dye for visualization of the droplet-like puncta (100 nM JFX549, yellow). A white dashed line outlines the nucleus. (C) The mean residence time of TAF15(IDR)-Halo-FTH1 in its puncta is significantly longer than that of Halo-TAF15(IDR) in its puncta. The value for each protein is averaged from 20 cells measured in 3 independent transfection and imaging sessions. Error bars represent standard errors. Asterisk indicates a significant difference between the two proteins (P < 0.05, Wilcoxon rank-sum test).

Figure 6 - source data 1. RTs measured by SPT used to generate the bar plots.
Download Figure 6 - source data 1.xlsx

Video 2. **A two-color real-time movie of individual TAF15(IDR)-Halo-FTH1 molecules binding to its puncta.**
Download Video2.AVI

296

Discussion

Understanding situations in which PFA fixation can properly preserve live-cell conditions is essential in judicious applications of fixation-based biological techniques. Because approaches for rigorous determination of LLPS *in vivo* remain lacking (McSwiggen et al., 2019b) and detection of local high-concentration regions of an endogenously expressed protein in fixed cells via immunofluorescence has been widely used as evidence for LLPS (Hayes and Weeks, 2016; Kato et al., 2012; Lin et al., 2016; Maharana et al., 2018; Sabari et al., 2018; Wang et al., 2021; Yang et al., 2020), understanding how well fixation preserves LLPS behaviors is important for justifying the immunofluorescence-based diagnosis method and for studying the functional relevance of LLPS *in vivo*. In this work, we imaged various LLPS systems in living cells before and after PFA fixation, quantified parameters that describe LLPS

307   appearance in cells, and showed that fixation can either enhance or diminish the apparent LLPS

308   behaviors *in vivo*. Lowering the PFA concentration and adding GA to PFA did not remove the fixation

309   artifacts. For the first time, our work reveals an important caveat in using fixation-based methods to

310   detect and characterize LLPS *in vivo* and suggests an advantage of using live-cell imaging to study LLPS

311   systems over fixed-cell experiments. However, not all the proteins we examined have their puncta-

312   forming or apparent LLPS behaviors in cells changed upon fixation. For example, PFA fixation faithfully

313   preserves the appearance of FUS(FL), TAF15(IDR)-FTH1, and EWS::FLI1 puncta in cells (**Figure 3**).

314   Nevertheless, our work points out a necessity to use live-cell imaging to confirm LLPS behaviors

315   previously characterized with fixed-cell experiments. Live imaging techniques that allow estimation of

316   protein diffusion coefficients within specific cellular compartments, e.g., SPT (Hansen et al., 2018 and

317   Heckert et al., 2022) and fluorescence correlation spectroscopy (Lanzanò et al., 2017), can be useful

318   alternative approaches for diagnosing LLPS *in vivo* without the potential artifact of fixation, as diffusion

319   dynamics are recently shown to be affected by LLPS (Heltberg et al., 2021; McSwiggen et al., 2019a;

320   Miné-Hattab et al., 2021; Chong et al., 2022; and Ladouceur et al., 2020).

321   We note that fixation-induced changes of LLPS appearance may lead to potential

322   misinterpretation of the functional relevance of LLPS in cellular processes. For example, recent work has

323   uncovered that effective transcriptional activation requires an optimum of TF IDR-IDR interactions

324   within TF hubs formed at target genes and that overly high levels of IDR-IDR interactions pushing the

325   system toward LLPS can repress transcription (Chong et al., 2022 and Trojanowski et al., 2022). Future

326   characterization of the functionally optimal interaction level will require quantification of the sizes of

327   hubs or droplet-like puncta while measuring transcription activity. Because a fixation-induced increase

328   or decrease in puncta sizes may lead to inaccurate determination of the functional optimum, scrutiny

329   will be required in choosing between live-cell and fixed-cell imaging methods for quantifying LLPS

330   appearance in these types of studies. Moreover, given that fixation can artificially generate intranuclear

331   puncta of EGFP-EWS(IDR) that is homogenously distributed across the live cell nucleus (**Figure 1A**), extra

332   caution is required in interpreting immunofluorescence-detected intracellular puncta of an

333   endogenously expressed protein as LLPS, as the same puncta-generating fixation artifact might happen

334   to the protein even when it is not phase separating in living cells. To confirm puncta formation,

335   counterpart live-cell imaging of the endogenous protein will be necessary, which requires engineering

336   the cells, e.g., by CRISPR, to fluorescently tag the protein.

337   To understand the factors that can cause fixation-induced changes of LLPS appearance in the

338   cell, we simulated the changes through kinetic modeling, which reveals that the dynamics of POI binding

339   to and dissociating from puncta, the absolute fixation rate of POI, and different fixation rates of POI in

340   and out of puncta all play a role in inducing the fixation artifacts. Our kinetic model takes previous work

341   studying fixation artifacts in the context of protein-DNA interactions (Poorey et al., 2013; Schmiedeberg

342   et al., 2009; Teves et al., 2016) one step further by considering two fixed states of POI instead of one

343   state, which are fixation in and out of puncta with different rates due to distinct local protein

344   composition and concentrations. We then used live-cell single-molecule imaging experiments to

345   demonstrate that as predicted by our model, a fast overall fixation rate of POI relative to its puncta-

346   binding dynamics can minimize fixation artifacts.

347   We emphasize that because our four-state model makes no assumptions about any state being

348   phase-separated, the logical implications of our model can extend beyond LLPS to other biomolecular

349   transactions and cellular structures that have been found not well preserved by fixation or

350 immunofluorescence, including localizations of cilia proteins (Hua and Ferland, 2017), clustering of cell
351 membrane receptors (Stanly et al., 2016), splicing speckle formation (Neugebauer and Roth, 1997), and
352 chromatin organization and protein binding (Zarębski et al., 2021; Lorber and Volk, 2022; Lerner et al.,
353 2016; Pallier et al., 2003; Kumar et al., 2007; and Teves et al., 2016). Our model can similarly extend
354 beyond PFA to other fixatives. This is useful because different fixatives have been chosen for studying
355 different types of structures. For example, PFA fixation is often preferable for preserving soluble
356 proteins over dehydration fixatives such as methanol (Stadler et al., 2010 and Schnell et al., 2012), yet
357 methanol fixation can be preferable over PFA for preserving proteins bound to mitotic chromatin
358 (Kumar et al., 2007 and Lerner et al., 2016). Generally, our model predicts that fixation artifacts will
359 occur whenever a protein can exist in multiple states that have different rates of fixation, and this
360 artifact is most severe when the fixation is slower than the transition between states. For PFA fixation,
361 because its rate is sensitively dependent on the amino acid sequence of POI, the structure of POI, and
362 POI's cross-linked partners (Hoffman et al., 2015; Kamps et al., 2019; Metz et al., 2006; Metz et al.,
363 2004), POI in different states likely has different PFA fixation rates regardless of the type of interaction it
364 undergoes.

365 One distinction between our study and previous studies is that we observe that PFA fixation can
366 enhance apparent protein-protein interactions or LLPS behaviors in the cell, suggesting faster fixation
367 for POI in the bound than dissociated state ($k_3 > k_4$), whereas fixation has only been reported to
368 diminish protein-DNA interactions, suggesting slower fixation for POI in the bound state ($k_3 < k_4$)
369 (Poorey et al., 2013; Schmiedeberg et al., 2009; Teves et al., 2016). We hypothesize that this is because
370 fixing the bound state of an LLPS system (within puncta) is dominated by cross-linking reactions
371 between IDRs enriched in puncta, which have reactive residues better exposed to solvent due to lack of
372 well-defined tertiary structures and thereby likely cross-link faster than structured domains cross-linking
373 to DNA (Hoffman et al., 2015). It will be of future interest to measure fixation rates of different
374 biomolecules including IDRs, structured proteins, and nucleic acids to prove the proposed chemical
375 mechanism underlying fixation artifacts. Since our simulated results highlight the role of absolute
376 fixation rates in the outcome of fixation, another future endeavor will be to design novel fixatives with
377 significantly faster cross-linking rates than biomolecular interactions to eliminate fixation artifacts in the
378 cell.

379

380 **Materials and Methods**

Key Resources Table				
Reagent type (species) or resource	**Designation**	**Source or reference**	**Identifiers**	**Additional information**
cell line (human)	Knock-in A673 cell line	Chong et al., 2018	N/A	Human: A673 carrying HaloTag knock-in at the ews::fli1 locus

16

cell line (human)	U2OS cell line	Chong et al., 2018	N/A	N/A
recombinant DNA reagent	EGFP-EWS(IDR)-NLS	This paper	N/A	Plasmid encoding the protein. See materials availability statement.
recombinant DNA reagent	EGFP-FUS(IDR)-NLS	This paper	N/A	Plasmid encoding the protein. See materials availability statement.
recombinant DNA reagent	EGFP-TAF15(IDR)-NLS	This paper	N/A	Plasmid encoding the protein. See materials availability statement.
recombinant DNA reagent	DsRed2-TAF15(IDR)-NLS	This paper	N/A	Plasmid encoding the protein. See materials availability statement.
recombinant DNA reagent	Halo-TAF15(IDR)-NLS	Chong et al., 2018	N/A	Plasmid encoding the protein. See materials availability statement.
recombinant DNA reagent	EGFP-FUS(FL)	This paper	N/A	Plasmid encoding the protein. See materials availability statement.
recombinant DNA reagent	NLS-TAF15(IDR)-Halo-FTH1	This paper	N/A	Plasmid encoding the protein. See materials availability statement.
chemical compound, drug	Glycine	Fisher Scientific	Fischer Scientific: BP381-5	N/A
chemical compound, drug	Paraformaldehyde	VWR	VWR: 100503-917	N/A
chemical compound, drug	Glutaraldehyde	Sigma-Aldrich	Sigma-Aldrich: 340855-25ML	N/A

381

Cell Line and Sample Preparation. U2OS cells were grown in 1 g/L DMEM media (ThermoFisher, 10567014) supplemented with 10% FBS (Fisher Scientific, SH3039603) and 1% penicillin-streptomycin (ThermoFisher, 15140122). The cells were split onto an imaging plate (Mattek, P35G-1.5-14-C) and transfected with fluorescent protein constructs with Lipofectamine 3000 (Fisher Scientific, L3000001)

17

386   according to manufacturer's instructions. One day after transfection, the culture media was changed to

387   phenol-red-free DMEM (ThermoFisher, 11054001) with 10% FBS and 1% penicillin-streptomycin. For

388   experiments with additional glycine, glycine (Fisher Scientific, BP381-5) was added to the phenol red

389   free media so that the final concentration was 50 mM (and 25 mM after the addition of 8% PFA, see

390   below). It should be noted that normal DMEM media already contains 0.4 mM glycine. The knock-in

391   A673 cell line expressing endogenous EWS::FLI1-Halo (Chong et al., 2018) was grown in 4.5 g/L DMEM

392   media (ThermoFisher, 10566016) with 10% FBS (Fisher Scientific, SH3039603) and 1% penicillin-

393   streptomycin (ThermoFisher, 15140122). The cells were similarly split onto an imaging plate (Mattek,

394   P35G-1.5-14-C) and the culture media was changed to phenol-red-free DMEM (ThermoFisher,

395   31053028) just before imaging. The U2OS cell line used here was validated by whole-genome

396   sequencing as described in (Hansen et al., 2017). The knock-in A673 cell line was generated by genome

397   editing of the A673 cell line that was comprehensively authenticated by ATCC before distribution (ATCC,

398   CRL-1598). By the time that the A673 cells had been genome-edited and used in this work, they had

399   been cultured for 15 passages since purchased from ATCC. The genomic sequence of the locus encoding

400   EWS::FLI1-Halo in the knock-in A673 cell line was confirmed by Sanger sequencing. Both U2OS and A673

401   cell lines were tested for mycoplasma using PCR-based assays in February 2022.

402   **Fluorescence Microscopy.** Confocal fluorescence microscopy was performed on Zeiss LSM 980 in the

403   point-scanning mode with a 63x oil objective (Zeiss, 421782-9900-000). The pinhole was set to 1 airy

404   unit for different emission wavelengths. The images displayed in the manuscript are maximum z-

405   projections of z-stack images. A673 cell expressing endogenous EWS::FLI1-Halo were imaged in the

406   Airyscan mode of the same Zeiss LSM 980 microscope. All postprocessing parameters in the Airyscan

407   analysis module were kept constant to guarantee a fair comparison between the images taken before

408   and after fixation. The culture dish contained 1 mL of phenol red free media, so that when 1 mL of 8%

409   paraformaldehyde (PFA) (VWR, 100503-917) in PBS buffer was added to the dish, the final concentration

410   of PFA was 4%. To achieve final PFA concentrations of 1%, 2%, and 8%, 1 mL of 2%, 4%, and 16% of PFA

411   were diluted in PBS buffer and added to the culture dishes containing 1 mL of phenol red free media. A

412   final concentration of 0% was achieved by following the same protocol only using 1 mL of PBS buffer in

413   place of PFA. To achieve final concentration of 4% PFA with 0.2% glutaraldehyde (GA) (Sigma-Aldrich,

414   340855-25ML), 1 mL of 8% PFA with 0.4% GA in PBS buffer was added to the culture dishes. After

415   waiting 10 mins to allow PFA or PFA/GA fixation to complete, images of the same cells are taken again.

416   For experiments with glycine, the final concentration of glycine after PFA addition was 25 mM and 8%

417   PFA was used so that PFA was still in molar excess. Independent transfection and imaging sessions were

418   performed on different days using different plates of cells.

419   **LLPS Parameter Quantification.** The three parameters we quantified were the number of puncta,

420   surface roughness, and punctate percentage. The source code used to analyze the images is provided as

421   a supplementary file "Puncta Quantification Processing Scripts.zip". To best compare the images of a cell

422   before and after fixation, the two z-projection images were normalized so that the sum of the intensities

423   within the nucleus is equal to 1. The border of the nucleus was manually drawn for each image. All

424   analysis is done on normalized maximum z-projection images except for when calculating punctate

425   percentage. We measured the number of puncta by quantifying the number of peaks within the

426   nucleus. Specifically, the image was exported from MATLAB into ImageJ (Schindelin et al., 2012) using

427   MIJ (Sage et al., 2012), and the "find maxima" processing function was used (**Figure 7**) with the same

428   noise tolerance for both the live and fixed cell images.

18

429 To quantify the surface roughness of a cell nucleus image, the standard deviation of fluorescence
430 intensities in the nucleus were compared before and after fixation (**Figure 8**). Utilizing this method of
431 comparing images before and after fixation allows for quantification of change of nucleoplasm without
432 peak fitting. The addition of structures such as puncta within a chosen patch will increase the standard
433 deviation. Nuclei with puncta resulted in skewed (non-normal) distributions of intensities (Jachowicz et
434 al., 2021), leading to higher standard deviations.

435 The punctate percentage was determined with the first few steps identical to measuring the number of
436 puncta as described above. The border of the nucleus was manually identified, the images were
437 normalized, and preliminary peak locations were identified on maximum z-projection images using the
438 "find maxima" function in ImageJ. The "find maxima" function does not pick the perfect center of each
439 punctum. Thus, to measure the full width at half maximum (FWHM) of a punctum, we made 36 different
440 radial slices of the punctum crossing the preliminary punctum center pixel, extracted the intensity
441 profile for each radial slice to calculate the punctum's FWHM, and selected the highest FWHM as the
442 corresponding radial slice must have gone through the true center of the punctum. We then made a
443 sum z-projection of the z-stack images, drew a circle with the maximum FWHM as its diameter centering
444 the true central pixel of each punctum on the sum image, and integrated the fluorescence intensity
445 across all circles. (**Figure 9**). The punctate percentage is calculated by dividing the in-circle total
446 fluorescence intensity with the total fluorescence intensity integrated across the nucleus in the sum
447 image.
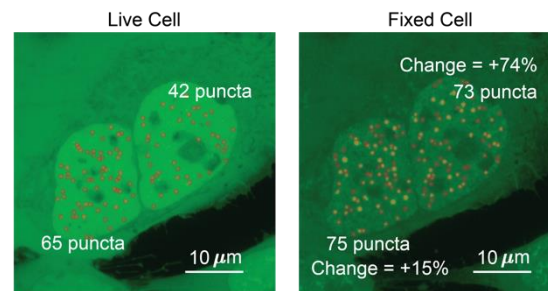
Figure 7. Determination of the number of puncta in the cell nucleus. Two cells expressing EGFP-TAF15(IDR) have the number of puncta before and after fixation compared. The cell on the left shows an increase of 10 puncta, a change of 15%. The cell on the right shows a change of 31 puncta, a change of 74%.
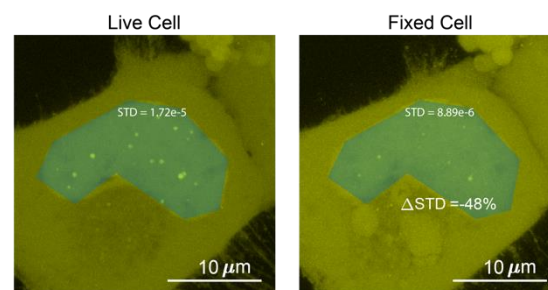
448

Figure 8. Determination of the surface roughness of a cell nucleus image. We drew a blue patch that covers the nucleus of a cell expressing Halo-TAF15(IDR) and compared the standard deviation of the

pixel intensity within the blue patch before and after fixation. The change in standard deviation between the two images is -48%.
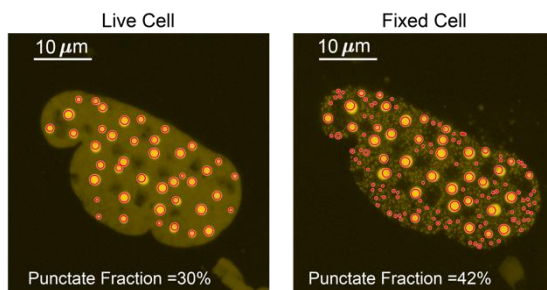
449

Figure 9. Determination of the punctate percentage. The punctate percentage of DsRed2-TAF15(IDR) is compared before and after fixation. The red circles represent the boundary within which the integrated fluorescence is considered "in puncta".

Source Code 1. **Code used to quantify number of puncta, surface roughness of cell nucleus, and punctate percentage**

450   Download Puncta Quantification Processing Scripts.zip

451

452   **Kinetic Simulation.** A four-state kinetic model was constructed in COPASI (Hoops et al., 2006) and
453   interfaced using Python. The complete iPython notebook containing the source code used to perform
454   the simulation is provided a supplementary file "Kinetic Simulation.zip". The four states and kinetic rates
455   are defined in the main text and **Figure 5B**. We assume a constant total molarity for all species, i.e.,
456    $[S_1] + [S_2] + [S_3] + [S_4] = 1 \, mol/L$. At $t = 0$, $[S_3] = [S_4] = 0$, while k_1 and k_2 together define the
457   equilibrium between S_1 and S_2, i.e., $K_{eq} = k_1/k_2 = [S_1]_{eq}/[S_2]_{eq}$. COPASI numerically simulates the
458   four states in the kinetic model utilizing the starting concentrations and rate conditions.

459   The units used for all the rates were s^{-1}, set so that fixation occurred on the order of seconds. For the
460   simulations that produced **Figure 5C**, we varied the values of k_3 and k_4 but kept the total fixation and
461   POI binding and dissociation rates constant ($k_3 + k_4$ = 0.2, $k_1 + k_2 = 1$), leading to a constant relative
462   overall fixation rate of POI ($(k_3 + k_4):(k_1 + k_2)$=1:5). For the simulations that produced **Figure 5D**, we
463   kept the fixation rates constant ($k_3 = 1$, $k_4 = 2$) and varied the relative overall fixation rate of POI
464   ($(k_3 + k_4):(k_1 + k_2)$). In this simulation, the relative overall fixation rate of POI ($(k_3 + k_4):(k_1 + k_2)$)
465   is set so that the range of interaction rates span values that are an order of magnitude faster and slower
466   than fixation rates.

Source Code 2. **Code used to perform kinetic simulation of the four-state fixation model**

467   Download Kinetic Simulation.zip

468   **Single-particle Tracking (SPT).** SPT of Halo-tagged TAF15(IDR) and TAF15(IDR)-FTH1 were performed on
469   a Nikon Eclipse Ti2 TIRF microscope with a 100x/NA 1.49 oil-immersion objective (CFI SR HP Apochromat
470   TIRF 100XAC Oil) under highly inclined and laminated optical sheet (HILO) illumination (Tokunaga et al.,
471   2008). PA-JF646 was activated and excited under variable powers by 405 nm and 640 nm laser lines,

472 respectively, while JFX549 was excited by a 561 nm laser line. The incubation chamber was held
473 humidified at a 37°C with 5% CO_2 and the objective was also heated to 37°C.

474 Halo-tagged TAF15(IDR) and TAF15(IDR)-FTH1 were overexpressed in U2OS cells and stained with 100
475 nM JFX549 and 20 nM PA-JF646. Droplet-like puncta were visualized in the JFX549 channel, while
476 individual molecules detected in the PA-JF646 channel were tracked in real-time. A low 405 nm
477 activation power was used to ensure sufficiently sparse activation of PA-JF646-labeled proteins and
478 allow for SPT. For SPT in the PA-JF646 channel, long camera exposure time (500 ms per frame, 2000
479 frames) blurred out faster diffusing molecules and ensured that we only detect bound molecules. In the
480 JFX549 channel, time-lapse images (500 ms per frame, one frame every 10 seconds) were taken to track
481 the location of droplet-like puncta during the entire acquisition while limiting the effects of
482 photobleaching.

483 The analysis was performed following (Chong et al., 2018) and is briefly described below. Single-
484 molecule data from the PA-JF646 channel was analyzed using a SLIMfast (Sergé et al., 2008), a GUI based
485 on a MATLAB implementation of the MTT algorithm (Normanno et al., 2015), and is available in the
486 supplemental materials of (Teves et al., 2016). SPT analysis was performed using the following
487 parameters: localization error: 10^{-6}; deflation loops: 3; maximum number of competitors: 5; maximal
488 expected diffusion constant (μm^2/s): 0.1.

489 Binary masks of the droplet-like puncta were generated from the JFX549 channel using custom-written
490 Macros in ImageJ from (Chong et al., 2018). Using custom-written MATLAB code also from (Chong et al.,
491 2018), single-molecule trajectories were then sorted into in-puncta and out-of-puncta trajectories based
492 on the fraction of time a molecule spent in the punctum, F. A trajectory with F > 50% was considered in-
493 puncta and one with F < 5% was considered out-of-puncta. We only focused on the in-puncta
494 trajectories.

495 Survival probability curves were then generated from the in-puncta trajectories and fit to the following
496 two-component exponential model.

$$P(t) = Ae^{-k_1 t} + (1-A)e^{-k_2 t}, \tag{2}$$

$$1/k_1 = \tau_{ns}, 1/k_2 = \tau_s,$$

497 with τ_{ns} and τ_s as the specific and nonspecific residence times, respectively. Here, we only focused on
498 the specific residence times.

499 In order to correct for photobleaching (Hansen et al., 2017), the specific residence time of histone H2B
500 (which is largely immobile on the chromatin) was measured via SPT as described above, except on all
501 trajectories rather than doing the in-puncta and out-of-puncta classification. We used PA-JF646-tagged
502 H2B-Halo that was stably expressed in U2OS cells and imaged under illumination and acquisition
503 parameters identical to those used to image Halo-tagged TAF15 and TAF15-FTH1. The corrected specific
504 residence times of the Halo-tagged TAF15 and TAF15-FTH1 ($\tau_{\text{corrected}}$) were computed based on the
505 following model.

$$\tau_{\text{corrected}} = 1/(1/\tau_s - 1/\tau_{\text{H2B}}), \tag{3}$$

506 with τ_{H2B} as the specific residence time of H2B.

507 Independent experiments were performed across at least three days for both Halo-tagged TAF15 and
508 TAF15-FTH1. In each session, multiple movies of both constructs were taken along with three movies of
509 Halo-tagged H2B to perform correction for that specific day. We reported the mean corrected residence
510 times.

511 **Statistical Analysis.** Non-parametric tests used throughout because the data were often not normally
512 distributed. Statistical significance of the LLPS parameters was calculated using the Wilcoxon signed-
513 rank test and statistical significance of the residence times from SPT was using the Wilcoxon signed-rank
514 test (Gibbons and Chakraborti, 2014). The Wilcoxon signed-rank test and Wilcoxon rank-sum test were
515 performed using the built-in MATLAB functions *signrank* and *ranksum*, respectively.

516

525 **Conflict of Interests**

526 No competing interests declared.

527 **Materials Availability Statement**

528 The materials described in this study are available on request.

529 **References**

530 Alberti, S., Gladfelter, A., and Mittag, T. (2019). Considerations and challenges in studying liquid-liquid
531 phase separation and biomolecular condensates. Cell *176*, 419-434.
532 Altmeyer, M., Neelsen, K.J., Teloni, F., Pozdnyakova, I., Pellegrino, S., Grøfte, M., Rask, M.-B.D.,
533 Streicher, W., Jungmichel, S., and Nielsen, M.L. (2015). Liquid demixing of intrinsically disordered
534 proteins is seeded by poly (ADP-ribose). Nature communications *6*, 1-12.
535 Bellapadrona, G., and Elbaum, M. (2014). Supramolecular protein assemblies in the nucleus of human
536 cells. Angewandte Chemie *53*, 1534–1537.
537 Banani, S.F., Lee, H.O., Hyman, A.A., and Rosen, M.K. (2017). Biomolecular condensates: organizers of
538 cellular biochemistry. Nature reviews Molecular cell biology *18*, 285-298.
539 Berry, J., Weber, S.C., Vaidya, N., Haataja, M., and Brangwynne, C.P. (2015). RNA transcription
540 modulates phase transition-driven nuclear body assembly. Proceedings of the National Academy of
541 Sciences *112*, E5237-E5245.
542 Boeynaems, S., Alberti, S., Fawzi, N.L., Mittag, T., Polymenidou, M., Rousseau, F., Schymkowitz, J.,
543 Shorter, J., Wolozin, B., and Van Den Bosch, L. (2018). Protein phase separation: a new phase in cell
544 biology. Trends in cell biology *28*, 420-435.

545   Bracha, D., Walls, M.T., Wei, M.-T., Zhu, L., Kurian, M., Avalos, J.L., Toettcher, J.E., and Brangwynne, C.P.
546   (2018). Mapping local and global liquid phase behavior in living cells using photo-oligomerizable seeds.
547   Cell *175*, 1467-1480. e1413.
548   Chen, F., Tillberg, P.W., and Boyden, E.S. (2015). Expansion microscopy. Science *347*, 543-548.
549   Choi, J.-M., Holehouse, A.S., and Pappu, R.V. (2020). Physical principles underlying the complex biology
550   of intracellular phase transitions. Annual Review of Biophysics *49*, 107-133.
551   Chong, S., Dugast-Darzacq, C., Liu, Z., Dong, P., Dailey, G.M., Cattoglio, C., Heckert, A., Banala, S., Lavis,
552   L., and Darzacq, X. (2018). Imaging dynamic and selective low-complexity domain interactions that
553   control gene transcription. Science *361*, eaar2555.
554   Chong, S., Graham, T.G.W., Dugast-Darzacq, C., Dailey, G.M., Darzacq, X., and Tjian, R. (2022). Tuning
555   levels of low-complexity domain interactions to modulate endogenous oncogenic transcription.
556   Molecular Cell.
557   Currie, S.L., and Rosen, M.K. (2022). Using quantitative reconstitution to investigate multicomponent
558   condensates. RNA *28*, 27-35.
559   Ganser, L.R., and Myong, S. (2020). Methods to study phase-separated condensates and the underlying
560   molecular interactions. Trends in biochemical sciences *45*, 1004.
561   Gavrilov, A., Razin, S.V., and Cavalli, G. (2015). In vivo formaldehyde cross-linking: it is time for black box
562   analysis. Briefings in functional genomics *14*, 163-165.
563   Gibbons, J.D., and Chakraborti, S. (2014). Nonparametric statistical inference (CRC press).
564   Gibbs, J.W. (1879). On the equilibrium of heterogeneous substances.
565   Graham, T. (1861). X. Liquid diffusion applied to analysis. Philosophical transactions of the Royal Society
566   of London, 183-224.
567   Grünewald, T., Cidre-Aranaz, F., Surdez, D., Tomazou, E. M., de Álava, E., Kovar, H., Sorensen, P. H.,
568   Delattre, O., and Dirksen, U. (2018). Ewing sarcoma. Nature reviews Disease primers *4*, 5.
569   Hansen, A. S., Pustova, I., Cattoglio, C., Tjian, R., and Darzacq, X. (2017). CTCF and cohesin regulate
570   chromatin loop stability with distinct dynamics. eLife *6*, e25776.
571   Hansen, A. S., Woringer, M., Grimm, J. B., Lavis, L. D., Tjian, R., and Darzacq, X. (2018). Robust model-
572   based analysis of single-particle tracking experiments with Spot-On. eLife *7*, e33125.
573   Hayes, M.H., and Weeks, D.L. (2016). Amyloids assemble as part of recognizable structures during
574   oogenesis in Xenopus. Biology open *5*, 801-806.
575   Heckert, A., Dahal, L., Tjian, R., and Darzacq, X. (2022). Recovering mixtures of fast-diffusing states from
576   short single-particle trajectories. eLife *11*, e70169.
577   Heltberg, M.L., Miné-Hattab, J., Taddei, A., Walczak, A.M., and Mora, T. (2021). Physical observables to
578   determine the nature of membrane-less cellular sub-compartments. eLife *10*, e69181.
579   Hoffman, E.A., Frey, B.L., Smith, L.M., and Auble, D.T. (2015). Formaldehyde crosslinking: a tool for the
580   study of chromatin complexes. Journal of Biological Chemistry *290*, 26404-26411.
581   Hoops, S., Sahle, S., Gauges, R., Lee, C., Pahle, J., Simus, N., Singhal, M., Xu, L., Mendes, P., and Kummer,
582   U. (2006). COPASI—a complex pathway simulator. Bioinformatics *22*, 3067-3074.
583   Hua, K., and Ferland, R.J. (2017). Fixation methods can differentially affect ciliary protein
584   immunolabeling. Cilia *6*, 1-17.
585   Hyman, A.A., Weber, C.A., and Jülicher, F. (2014). Liquid-liquid phase separation in biology. Annual
586   review of cell and developmental biology *30*, 39-58.
587   Jachowicz, J.W., Strehle, M., Banerjee, A.K., Thai, J., Blanco, M.R., and Guttman, M. (2021). Xist spatially
588   amplifies SHARP recruitment to balance chromosome-wide silencing and specificity to the X
589   chromosome.
590   Kamps, J.J., Hopkinson, R.J., Schofield, C.J., and Claridge, T.D. (2019). How formaldehyde reacts with
591   amino acids. Communications Chemistry *2*, 1-14.

592   Kato, M., Han, T.W., Xie, S., Shi, K., Du, X., Wu, L.C., Mirzaei, H., Goldsmith, E.J., Longgood, J., and Pei, J.
593   (2012). Cell-free formation of RNA granules: low complexity sequence domains form dynamic fibers
594   within hydrogels. Cell *149*, 753-767.
595   Kato, M., and McKnight, S.L. (2018). A solid-state conceptualization of information transfer from gene to
596   message to protein. Annual review of biochemistry *87*, 351-390.
597   Koga, S., Williams, D.S., Perriman, A.W., and Mann, S. (2011). Peptide–nucleotide microdroplets as a
598   step towards a membrane-free protocell model. Nature chemistry *3*, 720-724.
599   Kumar, S., Chaturvedi, N. K., Kumar, S., and Tyagi, R. K. (2008). Agonist-mediated docking of androgen
600   receptor onto the mitotic chromatin platform discriminates intrinsic mode of action of prostate cancer
601   drugs. Biochimica et biophysica acta *1783*, 59–73.
602   Kwon, I., Kato, M., Xiang, S., Wu, L., Theodoropoulos, P., Mirzaei, H., Han, T., Xie, S., Corden, J.L., and
603   McKnight, S.L. (2013). Phosphorylation-regulated binding of RNA polymerase II to fibrous polymers of
604   low-complexity domains. Cell *155*, 1049-1060.
605   Ladouceur, A. M., Parmar, B. S., Biedzinski, S., Wall, J., Tope, S. G., Cohn, D., Kim, A., Soubry, N., Reyes-
606   Lamothe, R., and Weber, S. C. (2020). Clusters of bacterial RNA polymerase are biomolecular
607   condensates that assemble through liquid-liquid phase separation. Proceedings of the National Academy
608   of Sciences of the United States of America *117*, 18540–18549.
609   Lanzanò, L., Scipioni, L., Di Bona, M., Bianchini, P., Bizzarri, R., Cardarelli, F., Diaspro, A., and Vicidomini,
610   G. (2017). Measurement of nanoscale three-dimensional diffusion in the interior of living cells by STED-
611   FCS. Nature communications *8*, 65
612   Lerner, J., Bagattin, A., Verdeguer, F., Makinistoglu, M. P., Garbay, S., Felix, T., Heidet, L., and Pontoglio,
613   M. (2016). Human mutations affect the epigenetic/bookmarking function of HNF1B. Nucleic acids
614   research *44*, 8097–8111.
615   Li, P., Banjade, S., Cheng, H.-C., Kim, S., Chen, B., Guo, L., Llaguno, M., Hollingsworth, J.V., King, D.S., and
616   Banani, S.F. (2012). Phase transitions in the assembly of multivalent signalling proteins. Nature *483*, 336-
617   340.
618   Lin, Y., Mori, E., Kato, M., Xiang, S., Wu, L., Kwon, I., and McKnight, S.L. (2016). Toxic PR poly-dipeptides
619   encoded by the C9orf72 repeat expansion target LC domain polymers. Cell *167*, 789-802. e712.
620   Lorber, D., and Volk, T. (2022). Evaluation of chromatin mesoscale organization. APL bioengineering *6*,
621   010902.
622   Magdalena Estirado, E., Mason, A.F., Alemán García, M.A.n., van Hest, J.C., and Brunsveld, L. (2020).
623   Supramolecular nanoscaffolds within cytomimetic protocells as signal localization hubs. Journal of the
624   American Chemical Society *142*, 9106-9111.
625   Maharana, S., Wang, J., Papadopoulos, D.K., Richter, D., Pozniakovsky, A., Poser, I., Bickle, M., Rizk, S.,
626   Guillén-Boixet, J., and Franzmann, T.M. (2018). RNA buffers the phase separation behavior of prion-like
627   RNA binding proteins. Science *360*, 918-921.
628   Matz, M.V., Fradkov, A.F., Labas, Y.A., Savitsky, A.P., Zaraisky, A.G., Markelov, M.L., and Lukyanov, S.A.
629   (1999). Fluorescent proteins from nonbioluminescent Anthozoa species. Nature biotechnology *17*, 969-
630   973.
631   McSwiggen, D.T., Hansen, A.S., Teves, S.S., Marie-Nelly, H., Hao, Y., Heckert, A.B., Umemoto, K.K.,
632   Dugast-Darzacq, C., Tjian, R., and Darzacq, X. (2019a). Evidence for DNA-mediated nuclear
633   compartmentalization distinct from phase separation. eLife *8*, e47098.
634   McSwiggen, D.T., Mir, M., Darzacq, X., and Tjian, R. (2019b). Evaluating phase separation in live cells:
635   diagnosis, caveats, and functional consequences. Genes & development *33*, 1619-1634.
636   Metz, B., Kersten, G.F., Baart, G.J., de Jong, A., Meiring, H., ten Hove, J., van Steenbergen, M.J., Hennink,
637   W.E., Crommelin, D.J., and Jiskoot, W. (2006). Identification of formaldehyde-induced modifications in
638   proteins: reactions with insulin. Bioconjugate chemistry *17*, 815-822.

639 Metz, B., Kersten, G.F., Hoogerhout, P., Brugghe, H.F., Timmermans, H.A., De Jong, A., Meiring, H., ten
640 Hove, J., Hennink, W.E., and Crommelin, D.J. (2004). Identification of formaldehyde-induced
641 modifications in proteins: reactions with model peptides. Journal of Biological Chemistry *279*, 6235-
642 6243.
643 Miné-Hattab, J., Heltberg, M., Villemeur, M., Guedj, C., Mora, T., Walczak, A.M., Dahan, M., and Taddei,
644 A. (2021). Single molecule microscopy reveals key physical features of repair foci in living cells. eLife *10*,
645 e60577.
646 Mitrea, D.M., and Kriwacki, R.W. (2016). Phase separation in biology; functional organization of a higher
647 order. Cell Communication and Signaling *14*, 1-20.
648 Moter, A., and Göbel, U.B. (2000). Fluorescence in situ hybridization (FISH) for direct visualization of
649 microorganisms. Journal of microbiological methods *41*, 85-112.
650 Neugebauer, K. M., and Roth, M. B. (1997). Distribution of pre-mRNA splicing factors at sites of RNA
651 polymerase II transcription. Genes and development *11*, 1148–1159.
652 Normanno, D., Boudarène, L., Dugast-Darzacq, C., Chen, J., Richter, C., Proux, F., Bénichou, O., Voituriez,
653 R., Darzacq, X., and Dahan, M. (2015). Probing the target search of DNA-binding proteins in mammalian
654 cells using TetR as model searcher. Nature communications *6*, 7357.
655 Nott, T.J., Petsalaki, E., Farber, P., Jervis, D., Fussner, E., Plochowietz, A., Craggs, T.D., Bazett-Jones, D.P.,
656 Pawson, T., and Forman-Kay, J.D. (2015). Phase transition of a disordered nuage protein generates
657 environmentally responsive membraneless organelles. Molecular cell *57*, 936-947.
658 Pallier, C., Scaffidi, P., Chopineau-Proust, S., Agresti, A., Nordmann, P., Bianchi, M. E., and Marechal, V.
659 (2003). Association of chromatin proteins high mobility group box (HMGB) 1 and HMGB2 with mitotic
660 chromosomes. Molecular biology of the cell *14*, 3414–3426.
661 Patel, A., Malinovska, L., Saha, S., Wang, J., Alberti, S., Krishnan, Y., and Hyman, A. A. (2017). ATP as a
662 biological hydrotrope. Science *356*, 753–756.
663 Pollard, T.D. (2010). A guide to simple and informative binding assays. Molecular biology of the cell *21*,
664 4061-4067.
665 Poorey, K., Viswanathan, R., Carver, M.N., Karpova, T.S., Cirimotich, S.M., McNally, J.G., Bekiranov, S.,
666 and Auble, D.T. (2013). Measuring chromatin interaction dynamics on the second time scale at single-
667 copy genes. Science *342*, 369-372.
668 Quinodoz, S.A., Ollikainen, N., Tabak, B., Palla, A., Schmidt, J.M., Detmar, E., Lai, M.M., Shishkin, A.A.,
669 Bhat, P., and Takei, Y. (2018). Higher-order inter-chromosomal hubs shape 3D genome organization in
670 the nucleus. Cell *174*, 744-757. e724.
671 Richter, K.N., Revelo, N.H., Seitz, K.J., Helm, M.S., Sarkar, D., Saleeb, R.S., d'Este, E., Eberle, J., Wagner,
672 E., and Vogl, C. (2018). Glyoxal as an alternative fixative to formaldehyde in immunostaining and
673 super‐resolution microscopy. The EMBO journal *37*, 139-159.
674 Rust, M.J., Bates, M., and Zhuang, X. (2006). Sub-diffraction-limit imaging by stochastic optical
675 reconstruction microscopy (STORM). Nature methods *3*, 793-796.
676 Sabari, B.R., Dall'Agnese, A., Boija, A., Klein, I.A., Coffey, E.L., Shrinivas, K., Abraham, B.J., Hannett, N.M.,
677 Zamudio, A.V., and Manteiga, J.C. (2018). Coactivator condensation at super-enhancers links phase
678 separation and gene control. Science *361*, eaar3958.
679 Sacchetti, A., Subramaniam, V., Jovin, T.M., and Alberti, S. (2002). Oligomerization of DsRed is required
680 for the generation of a functional red fluorescent chromophore. FEBS letters *525*, 13-19.
681 Sage, D., Prodanov, D., Tinevez, J.-Y., and Schindelin, J. (2012). MIJ: making interoperability between
682 ImageJ and Matlab possible. In ImageJ User & Developer Conference.
683 Schindelin, J., Arganda-Carreras, I., Frise, E., Kaynig, V., Longair, M., Pietzsch, T., Preibisch, S., Rueden, C.,
684 Saalfeld, S., and Schmid, B. (2012). Fiji: an open-source platform for biological-image analysis. Nature
685 methods *9*, 676-682.

686 Schnell, U., Dijk, F., Sjollema, K. A., and Giepmans, B. N. (2012). Immunolabeling artifacts and the need
687 for live-cell imaging. Nature methods *9*, 152–158.
688 Schmiedeberg, L., Skene, P., Deaton, A., and Bird, A. (2009). A temporal threshold for formaldehyde
689 crosslinking and fixation. PLoS One *4*, e4636.
690 Schuster, B.S., Dignon, G.L., Tang, W.S., Kelley, F.M., Ranganath, A.K., Jahnke, C.N., Simpkins, A.G., Regy,
691 R.M., Hammer, D.A., and Good, M.C. (2020). Identifying sequence perturbations to an intrinsically
692 disordered protein that determine its phase-separation behavior. Proceedings of the National Academy
693 of Sciences *117*, 11421-11431.
694 Sergé, A., Bertaux, N., Rigneault, H., and Marguet, D. (2008). Dynamic multiple-target tracing to probe
695 spatiotemporal cartography of cell membranes. Nature methods *5*, 687–694.
696 Shin, Y., and Brangwynne, C.P. (2017). Liquid phase condensation in cell physiology and disease. Science
697 *357*, eaaf4382.
698 Shishodia, S., Zhang, D., El-Sagheer, A., Brown, T., Claridge, T., Schofield, C., and Hopkinson, R. (2018).
699 NMR analyses on N-hydroxymethylated nucleobases–implications for formaldehyde toxicity and nucleic
700 acid demethylases. Organic & biomolecular chemistry *16*, 4021-4032.
701 Solomon, M.J., and Varshavsky, A. (1985). Formaldehyde-mediated DNA-protein crosslinking: a probe
702 for in vivo chromatin structures. Proceedings of the National Academy of Sciences *82*, 6470-6474.
703 Stadler, C., Skogs, M., Brismar, H., Uhlén, M., and Lundberg, E. (2010). A single fixation protocol for
704 proteome-wide immunofluorescence localization studies. Journal of Proteomics *73*, 1067-1078.
705 Stanly, T.A., Fritzsche, M., Banerji, S., García, E., Bernardino de la Serna, J., Jackson, D.G., and Eggeling, C.
706 (2016). Critical importance of appropriate fixation conditions for faithful imaging of receptor
707 microclusters. Biology Open *5*, 1343-1350.
708 Sutherland, B.W., Toews, J., and Kast, J. (2008). Utility of formaldehyde cross‐linking and mass
709 spectrometry in the study of protein‐protein interactions. Journal of mass spectrometry *43*, 699-715.
710 Teves, S.S., An, L., Hansen, A.S., Xie, L., Darzacq, X., and Tjian, R. (2016). A dynamic mode of mitotic
711 bookmarking by transcription factors. eLife *5*, e22280.
712 Tokunaga, M., Imamoto, N., and Sakata-Sogawa, K. (2008). Highly inclined thin illumination enables clear
713 single-molecule imaging in cells. Nature methods *5*, 159–161.
714 Trojanowski, J., Frank, L., Rademacher, A., Mücke, N., Grigaitis, P., and Rippe, K. (2022). Transcription
715 activation is enhanced by multivalent interactions independent of phase separation. Molecular cell *82*,
716 1878–1893.e10.
717 Wang, J., Choi, J.-M., Holehouse, A.S., Lee, H.O., Zhang, X., Jahnel, M., Maharana, S., Lemaitre, R.,
718 Pozniakovsky, A., and Drechsel, D. (2018). A molecular grammar governing the driving forces for phase
719 separation of prion-like RNA binding proteins. Cell *174*, 688-699. e616.
720 Wang, J., Shi, C., Xu, Q., and Yin, H. (2021). SARS-CoV-2 nucleocapsid protein undergoes liquid–liquid
721 phase separation into stress granules through its N-terminal intrinsically disordered region. Cell
722 discovery *7*, 1-5.
723 Yang, P., Mathieu, C., Kolaitis, R.-M., Zhang, P., Messing, J., Yurtsever, U., Yang, Z., Wu, J., Li, Y., and Pan,
724 Q. (2020). G3BP1 is a tunable switch that triggers phase separation to assemble stress granules. Cell *181*,
725 325-345. e328.
726 Yewdall, N.A., André, A.A., Lu, T., and Spruijt, E. (2021). Coacervates as models of membraneless
727 organelles. Current Opinion in Colloid & Interface Science *52*, 101416.
728 Yu, C., Shen, B., You, K., Huang, Q., Shi, M., Wu, C., Chen, Y., Zhang, C., and Li, T. (2021). Proteome-scale
729 analysis of phase-separated proteins in immunofluorescence images. Briefings in bioinformatics *22*,
730 bbaa187.
731 Zacharias, D.A., Violin, J.D., Newton, A.C., and Tsien, R.Y. (2002). Partitioning of lipid-modified
732 monomeric GFPs into membrane microdomains of live cells. Science *296*, 913-916.

733   Zarębski, M., Bosire, R., Wesołowska, J., Szelest, O., Eatmann, A., Jasińska-Konior, K., Kepp, O., Kroemer,
734   G., Szabo, G., and Dobrucki, J. W. (2021). Translocation of chromatin proteins to nucleoli-The influence
735   of protein dynamics on post-fixation localization. Cytometry. Part A : the journal of the International
736   Society for Analytical Cytology *99*, 1230–1239.
737   Zheng, W., Dignon, G.L., Jovic, N., Xu, X., Regy, R.M., Fawzi, N.L., Kim, Y.C., Best, R.B., and Mittal, J.
738   (2020). Molecular details of protein condensates probed by microsecond long atomistic simulations. The
739   Journal of Physical Chemistry B *124*, 11671-11679.

740

741